Nanoparticle-enabled increase of energy efficiency during laser metal additive manufacturing

Minglei Qu[1,2], Qilin Guo[1,2], Luis Izet Escano[1,2], Ali Nabaa[1,2], Kamel Fezzaa[3], Lianyi Chen[1,2,*]

[1]Department of Mechanical Engineering, University of Wisconsin-Madison, Madison, Wisconsin 53706, USA

[2]Department of Materials Science and Engineering, University of Wisconsin-Madison, Madison, Wisconsin 53706, USA

[3]X-ray Science Division, Argonne National Laboratory, Lemont, Illinois 60439, USA

*Corresponding author: lianyi.chen@wisc.edu

Corresponding author address: Department of Mechanical Engineering, University of Wisconsin-Madison, Madison, Wisconsin 53706, USA.

Abstract

The low energy efficiency of the laser metal additive manufacturing (AM) process is a potential sustainability concern for large-scale industrial production. Explicit investigation of the energy efficiency for laser melting requires the direct characterization of melt pool dimension and vapor depression, which is very difficult due to the opaque nature of the molten metal. Here we report the direct observation and quantification of effects of the TiC nanoparticles on the vapor depression and melt pool formation during laser powder bed fusion (LPBF) of Al6061 by in-situ high-speed high-energy x-ray imaging. Based on the quantification results, we calculated the laser melting energy efficiency (defined here as the ratio of the energy needed to melt the material to the energy delivered by the laser beam) with and without TiC nanoparticles during LPBF of Al6061. The results show that adding TiC nanoparticles into Al6061 leads to a significant increase

of laser melting energy efficiency (114% increase on average, 521% increase under 312 W laser power, 0.4 m/s scan speed). Systematic property measurement, simulation, and x-ray imaging studies enable us, for the first time, to identify that three mechanisms work together to enhance the laser melting energy efficiency: (1) adding TiC nanoparticles increases the absorptivity; (2) adding TiC nanoparticles decreases the thermal conductivity, and (3) adding TiC nanoparticles enables the initiation of vapor depression and multiple reflection at lower laser power (i.e., lowers the laser power threshold for keyholing). The method and mechanisms of using TiC nanoparticles to increase the laser melting energy efficiency during LPBF of Al6061 we reported here may guide the development of feedstock materials for more energy efficient laser metal AM.

Keywords: Additive manufacturing, laser powder bed fusion, energy efficiency, keyhole, melt pool, x-ray imaging, metal matrix nanocomposites

1. Introduction

Metal additive manufacturing (AM or 3D printing) is revolutionizing the manufacturing industry due to its advantages of manufacturing parts with complex geometries, reducing the need for tooling and part assembly, and shortening lead time [1–5]. However, the relatively low laser melting energy efficiency (here, is defined as the ratio of the energy needed to melt the material to the energy delivered by the laser beam, which is different from absorptivity, as detailed in Appendix A) during laser metal AM (especially for metals with high reflectivity and high thermal conductivity) is a potential sustainability concern for large-scale industrial production [6–9]. During laser metal AM, a large amount of laser energy was wasted, either via the reflection which may potentially damage the optical component [10,11], or via heat dissipation to coarsen microstructure in the heat-affected zone and degrade the mechanical properties [12,13]. Therefore,

more efficient use of laser energy cannot only benefit productivity, but also improve the equipment lifetime and product quality.

However, explicit study of the laser melting energy efficiency requires actual vapor depression (or called keyhole) and melt pool dimension [14,15], which are very difficult to be obtained by postmortem analysis due to the repeated overlapping of the scan tracks in the laser AM process [16,17]. It is also very difficult to directly visualize the vapor depression and melt pool formation due to the opaque nature of the molten metal. Conventional monitoring techniques, such as the visible light imaging [18,19] and thermography [20] can only capture information from the melt pool surface. Recently, x-ray imaging was applied to capture the vapor depression and melt pool dimension during laser melting [14,21,22]. Inline coherent imaging provides another way to capture the vapor depression depth during the laser melting process [23,24]. Although significant progress has been made in in-situ monitoring, reliable way to improve the laser melting energy efficiency beyond tuning laser processing parameters and the deep understanding of how to improve the laser melting energy efficiency during laser metal AM process have not been reported.

Previous studies have reported that adding nanoparticles can alter the properties (e.g., surface tension [25,26], viscosity [27,28], absorptivity [29–31], thermal conductivity [32], specific heat [33]) of metal matrix, which may potentially affect the melt pool volume and laser melting energy efficiency. However, most of the previous works studying the nanoparticle effects on laser melting (either by simulation or theoretical analysis) did not consider the changes of all these properties, due to the lack of measurement data [34–36]. So far, the quantitative understanding of which property change caused by the nanoparticles is the dominant factor in affecting both the melt pool volume and laser melting energy efficiency is lacking. During laser metal AM, vapor depression plays an important role in determining the laser absorption [37–39], which may significantly affect

the melt pool dimension. However, the effect of nanoparticles on the vapor depression formation has not been studied due to the difficulties in direct observation of the vapor depression during the laser metal AM process. Previous studies have demonstrated that adding nanoparticles in metal can increase the powder absorptivity (i.e., the absorptivity of the powder layer in LPBF) [30,40–43] and material absorptivity (i.e., the absorptivity of the flat surface) [10]. However, which absorptivity increase number should be used when studying nanoparticle effects on LPBF process is still unclear.

Here we report the direct observation and quantification of the effects of TiC nanoparticles on the vapor depression and melt pool formation during LPBF of Al6061 by in-situ high-speed high-energy x-ray imaging, and achieved a significant increase of laser melting energy efficiency (114% increase on average, 521% increase under 312 W laser power, 0.4 m/s scan speed) by TiC nanoparticles. Systematic property measurement, simulation, and x-ray imaging studies enable us, for the first time, to identify that three mechanisms work together to cause the laser melting energy efficiency enhancement: (1) adding TiC nanoparticles increases the absorptivity; (2) adding TiC nanoparticles decreases the thermal conductivity, (3) adding TiC nanoparticles enables the initiation of vapor depression and multiple reflection at lower laser power. Our method and mechanisms of using nanoparticles to increase the laser melting energy efficiency may guide the development of feedstock materials for more energy efficient laser metal AM.

2. Methods and materials

2.1. Materials

The Al6061 + 4.4 volume percentage of 83 nm TiC nanoparticles system, hereafter referred to as Al6061+4.4vol.%TiC, was used as a model system for this study [22,26,44]. The Al6061 powders (17-60 μm, D50: 34 μm) were purchased from Valimet (Stockton, CA, USA). The TiC

nanoparticles (83 nm) were purchased from SSnano (Houston, TX, USA). The Al6061 substrate was cut from commercial Al6061 plate (T6511) purchased from Mcmaster-Carr (Elmhurst, IL, USA). The Al6061+TiC powders were prepared by planetary ball milling (PQ-N04, Across International LLC, Livingston, NJ, USA) of the Al6061 powders with TiC nanoparticles. The Al6061+TiC substrate was prepared by LPBF of Al6061+TiC powders. A self-designed LPBF system was used for printing the Al6061+4.4vol.%TiC samples, which includes a continuous-wave ytterbium fiber laser (IPG YLR-500-AC, IPG Photonics, Oxford, MA, USA), a galvo scanner (hurrySCAN 30, SCANLAB GmbH., Puchheim, Germany), and a stainless steel vacuum chamber. The laser power used is 500 W. The scan speed is 0.2 m/s. The hatch spacing is 80 μm. The layer thickness is 50 μm. The laser beam diameter ($1/e^2$) is 239 ± 4 μm, which was measured by the knife edge method [45].

2.2. High-speed x-ray imaging

High-speed high-resolution x-ray imaging was performed at 32-ID beamline of the Advance Photon Source, Argonne National Laboratory. During the experiment, a continuous-wave laser beam irradiated the powder or substate surface to perform the laser melting experiment. The laser beam diameter (D4σ) is 94 ± 1 μm. The laser power of 208 W, 260 W, 312 W, 364 W, 416 W, 468 W and 520 W, and the scan speed of 0.4 m/s, 0.6 m/s and 0.8 m/s were used in the laser melting experiment. During laser melting, the x-ray penetrated through the laser melting region horizontally. The penetrated x-ray carrying the information of vapor depression and melt pool dimension was captured by a downstream high-speed camera at a frame rate of 50 kHz. The resolution of captured x-ray image is 1.93 μm per pixel. For the laser-powder bed melting experiment, the powder layer thickness is 100-120 μm. The laser melting energy efficiency change caused by the layer thickness variation of 20 μm is less than 8%, which is neglectable compared

with the average 114% increase in laser melting energy efficiency caused by nanoparticles. The substrate dimensions for both Al6061 and Al6061+4.4vol.%TiC are 40 mm long × 3 mm high × 0.7 mm thick (x-ray penetration direction). 0.7 mm substrate thickness is used because it is the best substrate condition for achieving (1) sufficient x-ray transparency, (2) fully containing the melt pool width, and (3) neglectable effects of thermal boundary condition on melt pool formation. The thickness for all the substrates is well controlled within 0.7 ± 0.01 mm range to ensure the consistent thermal boundary conditions for all the tests.

2.3. Quantification of vapor depression and melt pool dimension

The vapor depression dimensions (width and depth), melt pool width, and melt pool depth were quantified based on the x-ray images. Our x-ray imaging experiment always captured the middle length (1.5 mm) of the laser scan vector (2.5 mm) in laser melting experiments to avoid any acceleration or deceleration effects from scan mirrors at the starting or ending position of the scan path. Under certain processing parameters, the melt pool length is larger than the horizontal length of the x-ray imaging field of view and cannot be directly measured from a single x-ray image. For this case, the melt pool length was obtained by dividing it into two parts: (1) L_f, the length of melt pool portion displayed in the current field of view; (2) L_r, the length of the rest of melt pool beyond the field of view. To acquire L_f and L_r, two x-ray imaging frames are needed, as detailed in Appendix B. The melt pool width was quantified by measuring the solidified track width using optical microscope (Keyence VHX-5000 digital microscope, Keyence, Osaka, Japan). The average value and standard deviation were calculated and reported for all the dimension quantifications.

2.4. Computational thermo-fluid dynamics simulation

To find out the effects of thermophysical properties on the vapor depression and melt pool dimension, computational thermo-fluid dynamics simulation was performed by FLOW-3D

138 software (FLOW-3D 12.0, Flow Sciences, Santa Fe, NM, USA). Throughout the simulation, the
139 flow is assumed to be laminar and Newtonian. The governing equations are the continuity equation,
140 momentum conservation equation and energy conservation equation, as follows [46]:

141 $$\nabla (\rho \vec{\mathbf{v}}) = 0 \tag{1}$$

142 $$\frac{\partial}{\partial t}(\rho \vec{\mathbf{v}}) + \nabla (\rho \vec{\mathbf{v}} \otimes \vec{\mathbf{v}}) = \nabla (\mu \nabla \vec{\mathbf{v}}) - \nabla p + \rho \vec{\mathbf{g}} \tag{2}$$

143 $$\frac{\partial}{\partial t}(\rho h) + \nabla (\rho \vec{\mathbf{v}} h) = q + \nabla \cdot (k \nabla T) \tag{3}$$

144 where ρ is the density, $\vec{\mathbf{v}}$ is the velocity vector, t is the time, μ is the viscosity, p is the pressure, $\vec{\mathbf{g}}$
145 is the gravitational acceleration vector, k is the thermal conductivity, q is the heat source, h is
146 enthalpy, which is calculated as [46]:

147 $$h = \begin{cases} \rho_s C_s T, & T \le T_s \\ h(T_s) + h_{sl} \frac{T - T_s}{T_l - T_s}, & T_s < T \le T_l \\ h(T_l) + \rho_l C_l (T - T_l), & T > T_l \end{cases} \tag{4}$$

148 where ρ_s is the density in solid state, C_s is the specific heat in solid state, T is the temperature, h_{sl}
149 is the latent heat of melting, ρ_l is the density in liquid state, C_l is the specific heat in liquid state,
150 T_s is the solidus temperature, and T_l is the liquidus temperature.

151 The multiple reflection model based on the ray-tracing technique is implemented in the
152 simulation. For each incidence, absorption is calculated by the equation:

153 $$A = 1 - \frac{1}{2}\left(\frac{1 + (1 - \varepsilon\cos\theta)^2}{1 + (1 + \varepsilon\cos\theta)^2} + \frac{\varepsilon^2 - 2\varepsilon\cos\theta + 2\cos^2\theta}{\varepsilon^2 + 2\varepsilon\cos\theta + 2\cos^2\theta}\right) \tag{5}$$

154 where θ is the incident angle; and ε is a constant. The ε for Al6061 was calibrated by x-ray imaging
155 data (length and depth of melt pool, depth of vapor depression).

156 The driving forces including recoil pressure, thermocapillary force, gravity force and buoyancy
157 force are considered in the model. The recoil pressure is considered by the following equation:

$$P_r = 0.54 P_0 \exp\left[-\frac{\lambda}{K_B}\left(\frac{1}{T}-\frac{1}{T_b}\right)\right] \quad (6)$$

where P_0 is the ambient pressure, λ is the latent heat of vaporization, K_B is the Boltzmann constant, T is the surface temperature, and T_b is the boiling temperature.

The material properties (including density, specific heat, thermal conductivity, surface tension, viscosity, and absorptivity) used in the simulation are shown in Section 3.3. Other properties (solidus temperature, liquidus temperature, boiling temperature, latent heat of melting, latent heat of vaporization, and surface tension coefficient) can be found in reference [26]. The simulation domain is 3 mm (length) × 0.7 mm (thickness) × 0.5 mm (height). The initial temperature is 298 K.

2.5. Measurement of density

The density of Al6061 and Al6061+4.4vol.%TiC was measured by the Archimedes method. The measurements were performed at room temperature. The alcohol used in the measurement is 99% purity ethanol. The density of the sample was calculated based on the following equation:

$$\rho = \frac{W_A}{W_A - W_B}(\rho_0 - \rho_L) + \rho_L \quad (7)$$

where ρ is the density of the sample, W_A is the weight of the sample in air, W_B is the weight of sample in the ethanol, ρ_0 is the density of ethanol at the testing environment (789 kg/m^3 at 20 °C), and ρ_L is the density of air (1.2 kg/m^3). For both samples, the density was measured five times. The average value and standard deviation were reported.

2.6. Measurements of thermal diffusivity and specific heat

The thermal diffusivity and specific heat of Al6061 and Al6061+4.4vol.%TiC were measured by the laser flash method using NETZSCH LFA 467 equipment (Erich NETZSCH GmbH & Co, Selb, Germany). During the measurement, a light pulse was used to heat the front surface of the

square plate sample (12.7 mm (length) × 12.7 mm (width) × 1.8 mm (thickness)). The temperature increase of the rear surface as a function of time was recorded. The thermal diffusivity was calculated by the following equation:

$$a = 0.1388 \frac{b^2}{t_{0.5}} \tag{8}$$

where a is the thermal diffusivity, b is the sample thickness, and $t_{0.5}$ is the time required for the rear surface to reach half the maximum temperature.

In the laser flash experiment, the specific heat is inversely proportional to the maximum temperature of the rear surface. Therefore, the specific heat was determined by a comparison experiment. First, the maximum temperature of the rear surface for the reference sample (POCO graphite) was captured. Then the maximum temperature of the test sample (Al6061 or Al6061+4.4vol.%TiC) was measured under the same experimental conditions (sample dimension, graphite coating, laser power, and laser duration time) as the reference sample. The specific heat of the sample was determined by:

$$c_{p,\,s} = \frac{m_{\mathrm{r}} c_{p,\,\mathrm{r}} \Delta T_{\mathrm{r}}}{m_{\mathrm{s}} \Delta T_{\mathrm{s}}} \tag{9}$$

where m_{r} is the mass of the reference sample, $c_{p,\,\mathrm{r}}$ is the specific heat of the reference sample, ΔT_{r} is the temperature increase of the rear surface for the reference sample during the experiment, m_{s} is the mass of the test sample, and ΔT_{s} is the temperature increase of the rear surface for the test sample during the experiment.

For both Al6061 and Al6061+4.4vol.%TiC, the thermal diffusivity and specific heat were measured five times. The average value and standard deviation were reported.

2.7. Measurement of reflectivity

The reflectivity of the Al6061 and Al6061+4.4vol.%TiC bare plates at the wavelength range of 600-2000 nm was measured by the Perkin Elmer Lambda 19 UV/Vis/NIR spectrometer (PerkinElmer, Waltham, MA, USA). The step size is 2 nm. Before measurement, the Al6061 and Al6061+4.4vol.%TiC plates (32 mm length × 32 mm width × 5 mm thickness) were carefully grinded by silicon carbide sandpaper and polished down to 50 nm using water-based diamond suspension, followed by ultrasonic cleaning. For both materials, the reflectivity was measured three times to ensure the results are repeatable.

3. Results

3.1. Effects of nanoparticles on vapor depression and melt pool dimension

To quantify the laser melting energy efficiency, direct characterization of vapor depression and melt pool dimension was needed to calculate the melt pool volume and, thereby, laser melting energy efficiency. To characterize the vapor depression and melt pool dimension, we performed in-situ high-speed x-ray imaging experiments for Al6061 and Al6061+4.4vol.%TiC under various laser processing parameters (laser power of 312 W, 364 W, 416 W, 468 W and 520 W, scan speed of 0.4 m/s, 0.6 m/s and 0.8 m/s). The x-ray imaging and quantified results (Fig. 1, 2) show that for both Al6061 and Al6061+4.4vol.%TiC, increasing laser power altered the melting mode from conduction mode (i.e., without vapor depression) to keyhole mode (i.e., with vapor depression) and further increased the vapor depression (mainly depth) and melt pool dimension as the laser power increased. Comparing Al6061+4.4vol.%TiC with Al6061, adding TiC nanoparticles reduced the laser power required to generate the vapor depression. Under 0.4 m/s scan speed, the laser power required to generate the vapor depression for Al6061 is 416 W, while that for Al6061+4.4vol.%TiC is less than 312 W. The same trend was also observed at 0.6 m/s (520 W for Al6061 and 364 W for Al6061+4.4vol.%TiC to generate the vapor depression) and 0.8 m/s scan

speed (416 W for Al6061+4.4vol.%TiC to generate the vapor depression, while for Al6061, no vapor depression formed even with the highest laser power of 520 W). When the vapor depression was generated, under the same laser processing parameter (416 W, 0.4 m/s), adding nanoparticles significantly increased the vapor depression depth (190 ± 26 μm for Al6061, 324 ± 10 μm for Al6061+4.4vol.%TiC), the melt pool length (821 ± 7 μm for Al6061, 1781 ± 11 μm for Al6061+4.4vol.%TiC) and melt pool depth (228 ± 1 μm for Al6061, 390 ± 4 μm for Al6061+4.4vol.%TiC). For melt pool width, under most of the laser processing parameters we studied, adding nanoparticles increased the melt pool width, except for laser parameters with higher energy input (laser power of 468 W, 520 W, scan speed of 0.4 m/s), where we observed that adding TiC nanoparticles decreased the melt pool width.

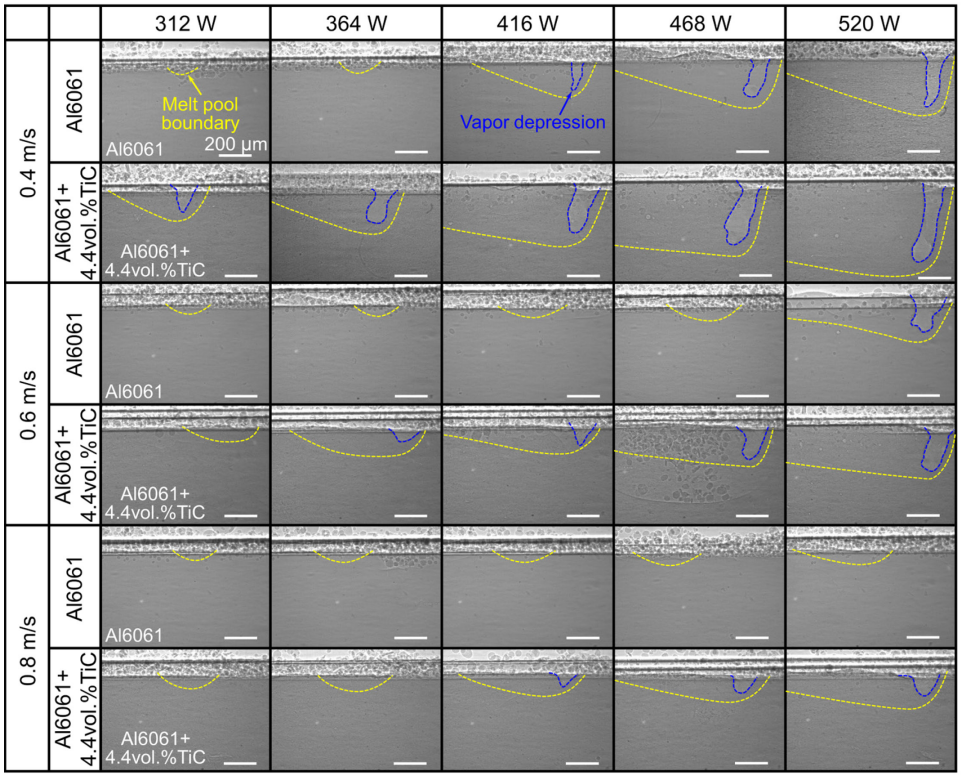

Fig. 1. X-ray images showing the effects of nanoparticles on the vapor depression and melt pool formation during LPBF process. *Under the same processing parameter, adding nanoparticles increased the vapor depression depth and melt pool dimension. Blue dashed lines indicate the vapor depression boundary. Yellow dashed lines indicate the melt pool boundary. The laser power*

used is 312 W, 364 W, 416 W, 468 W and 520 W. The scan speed used is 0.4 m/s, 0.6 m/s and 0.8 m/s. The materials are Al6061 and Al6061+4.4vol.%TiC.

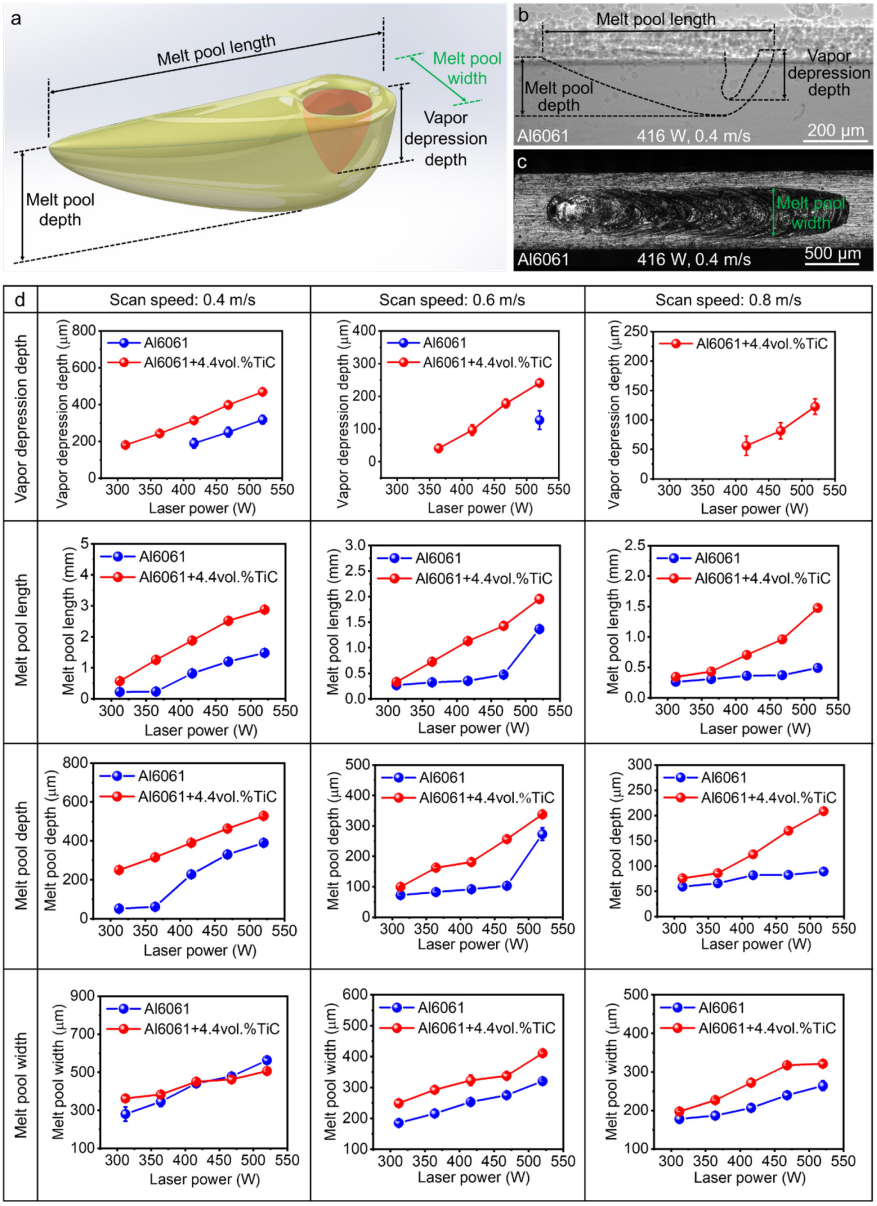

Fig. 2. Quantification of effects of nanoparticles on vapor depression and melt pool dimension during LPBF process. *(a) Schematic showing the vapor depression and melt pool dimensions. The red color represents the vapor depression. The yellow color represents the melt pool. (b) The vapor depression depth, melt pool length, and melt pool depth obtained based on the x-ray image. (c) The melt pool width obtained based on the optical image of solidified scan track. (d) Quantification results of the effects of nanoparticles on vapor depression depth, melt pool depth, melt pool length, and melt pool width during LPBF process. The error bars represent the standard deviation.*

3.2 Effects of nanoparticles on laser melting energy efficiency

Based on the vapor depression dimension and melt pool dimension, we calculated the melt pool volume and laser melting energy efficiency. The melt pool volume was calculated by subtracting the vapor depression volume (indicated by the red color in Fig. 2a) from the total melt pool volume (indicated by the yellow color in Fig. 2a) [14]. During the calculation, the vapor depression and melt pool were assumed in cone shape. Therefore, the vapor depression volume was calculated by:

$$V_v = \frac{S_v h_v}{3} = \frac{\pi d^2 h_v}{12} \tag{10}$$

where V_v is the vapor depression volume, S_v is the vapor depression opening area at top surface, h_v is the vapor depression depth, and d is the vapor depression width, as illustrated in Fig. 3a.

The total melt pool volume (including the vapor depression) was calculated by:

$$V_m = \frac{S_m h_m}{3} \tag{11}$$

where V_m is the total melt pool volume, h_m is the melt pool depth (Fig. 3a), S_m is the area of the melt pool top surface, which was calculated by (assuming the top surface of melt pool is elliptical):

$$S_m = \frac{\pi w L}{4} \tag{12}$$

where w is the melt pool width (Fig. 3b), and L is the melt pool length (Fig. 3a). Therefore, the real melt pool volume (V) was calculated by subtracting the vapor depression volume from the total melt pool volume:

$$V = V_m - V_v = \frac{\pi w L h_m}{12} - \frac{\pi d^2 h_v}{12} \tag{13}$$

The quantified results (Fig. 3c-e) show that adding nanoparticles significantly increased the melt pool volume. Under certain conditions of Al6061+4.4vol.%TiC with vapor depression but Al6061 without vapor depression, we saw one order of magnitude increase of melt pool volume (e.g.,

under 364 W laser power and 0.4 m/s scan speed, the melt pool volume of Al6061 is 1.3×10^{-12} m^3, while the melt pool volume of Al6061+4.4vol.%TiC is 3.8×10^{-11} m^3).

Based on the melt pool volume, the laser melting energy efficiency was calculated as:

$$\eta = \frac{E_m}{E_{in}} \tag{14}$$

where η is the laser melting energy efficiency, E_{in} is the energy delivered by the laser beam, which can be calculated as $E_{in} = Pt = PL/v$, where P is the laser power, t is the laser exposure time, L is the melt pool length, and v is the laser scan speed [14]. E_m is the energy required to melt the material, which includes the energy required to heat the material from the room temperature to the solidus temperature and the energy required to convert the material from the solid state to the liquid state (i.e., latent heat of melting), calculated using the following equation:

$$E_m = \rho V \int_{T_0}^{T_s} c_p \mathrm{d}T + \rho V (1-\omega) L_{Al} \tag{15}$$

where ρ is density of Al6061 or Al6061+TiC, V is the volume of the melt pool calculated according to Equation (10-13). c_p is the specific heat of Al6061 or Al6061+TiC, which were measured and will be detailed in Section 3.3. ω is the weight fraction of TiC (for Al6061, $\omega = 0$; for Al6061+4.4vol.%TiC, $\omega = 7.9\%$), L_{Al} is the latent heat of melting for Al6061 (3.4×10^5 J/kg), T_0 is the room temperature (298 K), and T_s is the solidus temperature of Al6061 (873 K).

The calculated results of laser melting energy efficiency show that adding TiC nanoparticles (Al6061+4.4vol.%TiC) increased the laser melting energy efficiency under all the laser processing conditions we investigated (Fig. 3f-h). Compared with Al6061, the average increase of laser melting energy efficiency caused by the TiC nanoparticles is 114% (from 4.9% to 10.5%) for all the laser parameters we studied. Under 312 W laser power and 0.4 m/s scan speed, adding TiC nanoparticles increases the laser melting energy efficiency by 521% (from 1.6% to 10.3%). This

suggested that adding nanoparticles can significantly improve the laser melting energy efficiency during LPBF process.

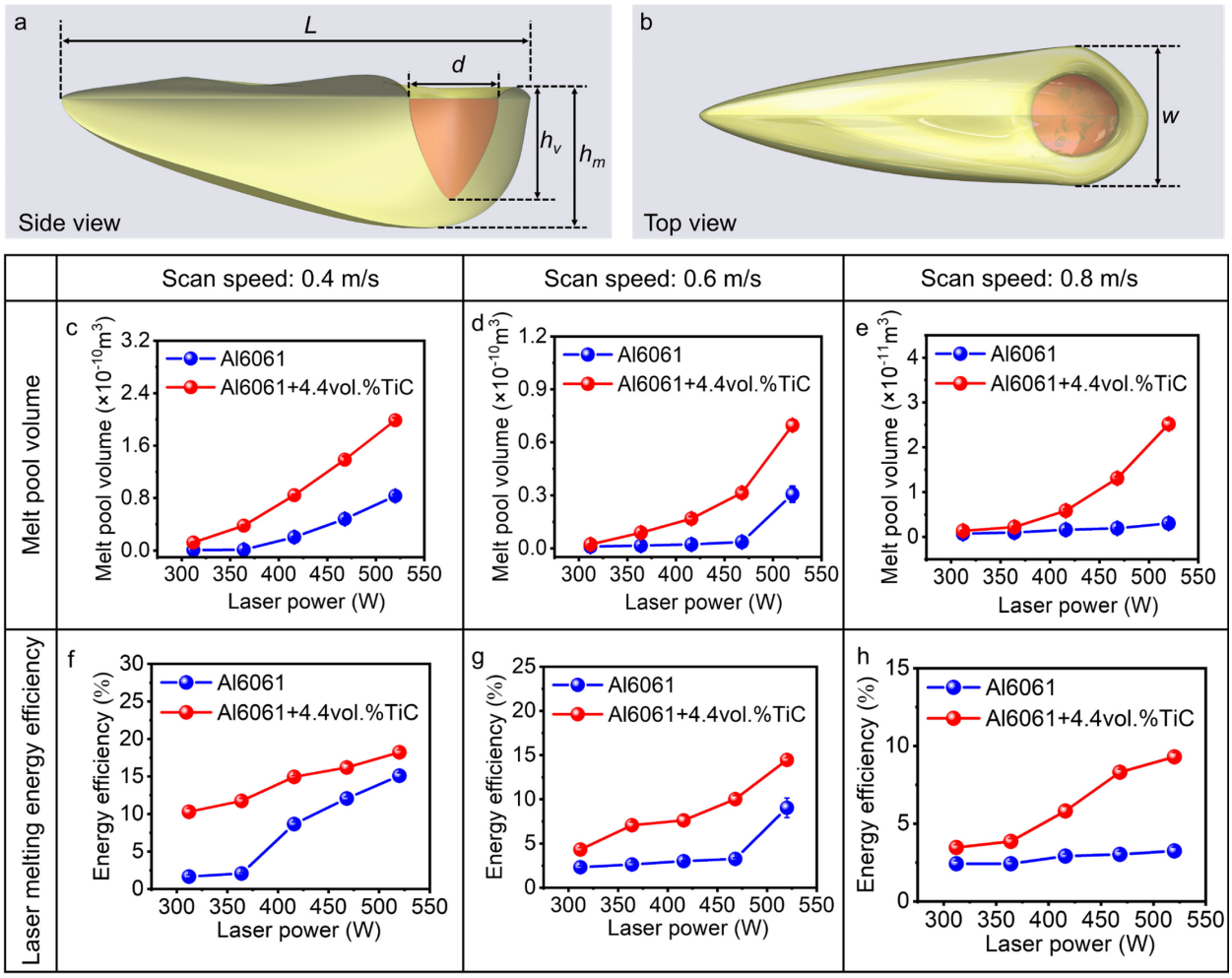

Fig. 3. Effects of nanoparticles on melt pool volume and laser melting energy efficiency. *(a) Side view of melt pool showing the required dimensions (melt pool length L, vapor depression width d, vapor depression depth h_v, melt pool depth h_m) for calculating the melt pool volume. (b) Top view of melt pool showing the melt pool width (w) for calculating the melt pool volume. (c-e) Effects of nanoparticles on the melt pool volume under laser scan speed of 0.4 m/s (c), 0.6 m/s (d), and 0.8 m/s (e). (f-h) Effects of nanoparticles on the laser melting energy efficiency under laser scan speed of 0.4 m/s (f), 0.6 m/s (g), and 0.8 m/s (h). The error bars represent the standard deviation.*

3.3. Effects of nanoparticles on properties

The nanoparticle-induced increase of laser melting energy efficiency may be attributed to the nanoparticle-induced change of material properties (e.g., specific heat, thermal conductivity, surface tension, viscosity, absorptivity), which may affect the heat transfer and melt pool dimension during laser metal AM process. However, due to the lack of systematic measurement, the quantitatively understanding of the effects of these property changes caused by nanoparticles on the melt pool volume and laser melting energy efficiency is unclear. In this study, we performed systematic measurements of the properties including density, specific heat, thermal conductivity, surface tension, viscosity, and absorptivity for Al6061 and Al6061+4.4vol.%TiC.

The density was measured by the Archimedes method. The measured density of Al6061 (commercial T6) is 2705 ± 3 kg m^{-3}. The measured density of as-printed Al6061+4.4vol.%TiC is 2801 ± 4 kg/m^3 (Fig. 4a). The increase of density was attributed to the higher density of TiC (4930 kg/m^3) than Al6061. According to the mixture rule, the density of fully dense Al6061+4.4vol.%TiC can be calculated as:

$$\rho_c=\rho_{Al}(1-f)+\rho_{TiC}f \tag{16}$$

where ρ_c is the density of Al6061+4.4vol.%TiC, ρ_{Al} is the density of Al6061, f is the volume fraction of TiC nanoparticles, and ρ_{TiC} is the density of TiC. The calculated density of fully dense Al6061+4.4vol.%TiC is 2802 kg m^{-3}. Therefore, the densification level of our as-printed Al6061+4.4vol.%TiC is 99.96%.

The specific heat and thermal diffusivity of Al6061 and Al6061+4.4vol.%TiC (at 298 K, 373 K, 473 K, 573 K, 673 K and 773 K) were measured by the laser flash analysis (Fig. 4b, c). The measured specific heat of Al6061 and Al6061+4.4vol.%TiC is very close (less than 10% difference for all temperatures), which can be attributed to the similar specific heat value of Al6061 and TiC [26,47]. The measured thermal diffusivity of Al6061+4.4vol.%TiC is 25% smaller (on average)

than that of the Al6061. Based on the density, specific heat and thermal diffusivity, the thermal conductivity of Al6061 and Al6061+4.4vol.%TiC was calculated using the equation [48]:

$$k = a\rho c_p \tag{17}$$

where k is the thermal conductivity, a is the thermal diffusivity, ρ is the density, c_p is the specific heat. The results show that the thermal conductivity of Al6061+4.4vol.%TiC is 24% (on average) lower than that of Al6061 (Fig. 4d). This can be attributed to: (1) the thermal conductivity of TiC is lower than that of Al6061 [49]; (2) the thermal resistance exists at the interface between the Al6061 and TiC nanoparticles [50].

The surface tension and viscosity were measured by the oscillating droplet method, as detailed in reference [26]. To minimize the effects of oxygen content variation on the testing results for different samples [51,52], we evacuated the chamber (less than 10 Pa for each iteration) and refilled with Argon gas (1.01×10^5 Pa for each iteration) three times to create a consistent clean environment for the oscillating droplet experiment for all the samples. The measured surface tension (Fig. 4e) of Al6061+4.4vol.%TiC (0.81 ± 0.06 N·m^{-1}) is 19% higher than that of the Al6061 (0.68 ± 0.03 N·m^{-1}). The measured viscosity (Fig. 4e) of Al6061+4.4vol.%TiC (79.4 ± 12.7 mPa·s) is 15 times higher than that of the Al6061 (4.9 ± 1.2 mPa·s).

To obtain the absorptivity, we first measured the reflectivity of Al6061 and Al6061+4.4vol.%TiC bare plates at wavelength of 600-2000 nm by the Perkin Elmer Lambda 19 UV/Vis/NIR spectrometer (see details in Method). Since the absorption lengths of Al and TiC at 1070 nm wavelength are much smaller (8.2 nm and 23.3 nm, respectively) [26] than the bare plate thickness, the absorptivity of Al6061 and Al6061+4.4vol.%TiC was then calculated by:

$$A = 1 - R \tag{18}$$

where A is the absorptivity, R is the reflectivity. The results (Fig. 4f) show that adding nanoparticles causes a 35% increase of the absorptivity from 0.051 for Al6061 to 0.069 for Al6061+4.4vol.%TiC at 1070 nm wavelength. Adding TiC nanoparticles increases the absorptivity because TiC has higher absorptivity than Al at 1070 nm wavelength [53,54]. Here we measured the bare plate absorptivity instead of powder absorptivity because bare plate absorptivity can better characterize the absorptivity of material itself with almost no geometric effects. We also estimated the material absorptivity of Al6061 and Al6061+4.4vol.%TiC based on the refractive index and Fresnel equations, as detailed in Appendix C. The estimated results are very close to the measured results, which further confirms the nanoparticle-induced increase of the material absorptivity.

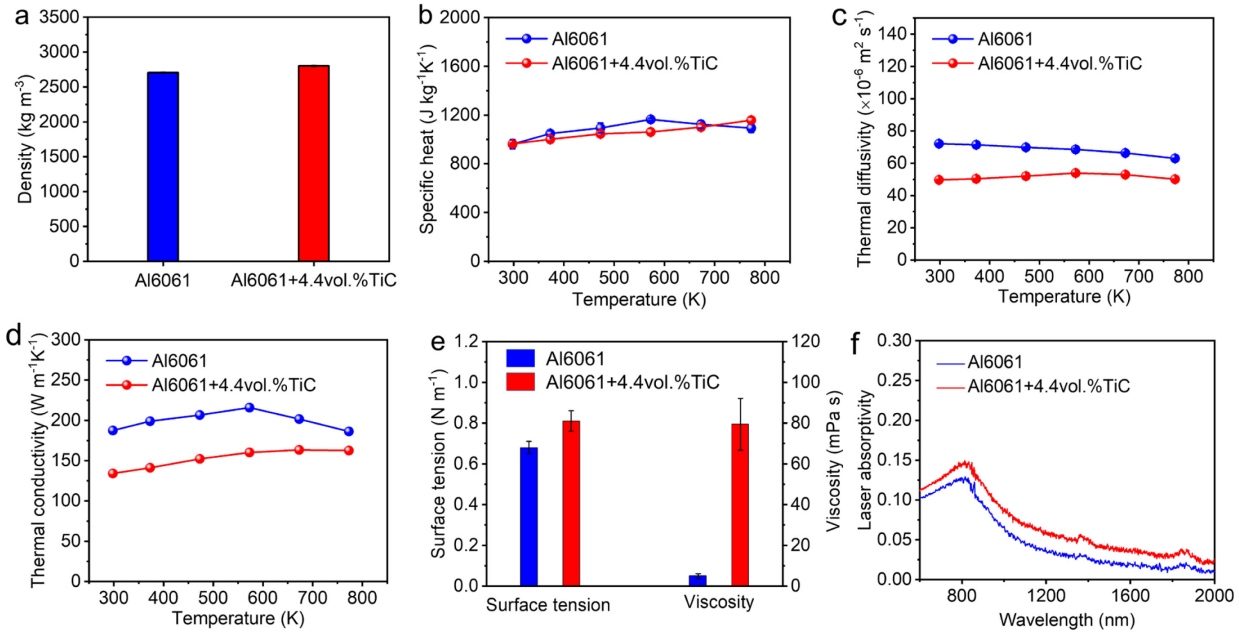

Fig. 4. Effects of nanoparticles on physical properties. *(a) Density of Al6061 and Al6061+4.4vol.%TiC. The density was measured by the Archimedes method. (b-d) Specific heat (b), thermal diffusivity (c) and thermal conductivity (d) of Al6061 and Al6061+4.4vol.%TiC. The specific heat and thermal diffusivity were measured by the laser flash method. The thermal conductivity was calculated based on the specific heat, thermal diffusivity and density. (e) Surface tension and viscosity of Al6061 and Al6061+4.4vol.%TiC. The surface tension and viscosity were measured by the oscillating droplet method. (f) The absorptivity of Al6061 and Al6061+4.4vol.%TiC. The error bars represent the standard deviation.*

4. Discussion

4.1. Effects of nanoparticle-induced property change on laser melting energy efficiency

The measured properties of Al6061 and Al6061+4.4vol.%TiC were input into simulation to study the effects of each property change caused by nanoparticles on the melt pool formation and laser melting energy efficiency. Totally six simulations were performed under the same laser processing condition (laser power of 416 W, laser scan speed of 0.4 m/s). The first simulation was the reference simulation using all the properties from Al6061 (Fig. 5a). The other five simulations (Fig. 5b-f) were performed with each simulation using one property (specific heat, thermal conductivity, surface tension, viscosity, absorptivity, or respectively) from Al6061+4.4vol.%TiC, while other properties were from Al6061. The results (Fig. 5g, h) show that nanoparticle-induced change of specific heat, thermal conductivity, surface tension, viscosity, and absorptivity results in a melt pool volume change of 6%, 71%, -11%, -7%, and 146%, respectively (negative means decrease). This suggested that the nanoparticle-induced change of the absorptivity and thermal conductivity are the two main reasons for the increase of the melt pool dimension observed in our experiment.

The decrease of the melt pool width after adding nanoparticles under the laser powers of 468 W and 520 W, scan speed of 0.4 m/s (mentioned in Section 3.1) may be because adding nanoparticles increases the viscosity [26], which impairs the thermocapillary flow and reduces the lateral spread of the liquid metal. Under certain condition with high energy input, the deep vapor depression causes more energy to be absorbed beneath the surface [14,55,56]. Therefore, the effect of nanoparticle-induced increase of absorptivity on the surface (tends to increase melt pool width) is diminished. The melt pool widening effect caused by the nanoparticle-induced increase of absorptivity and decrease of thermal conductivity was overcame by the narrowing effect caused

by the nanoparticle-induced increase of viscosity. This explained why under certain parameters (with higher energy input), we observed that adding nanoparticles decreased the melt pool width.

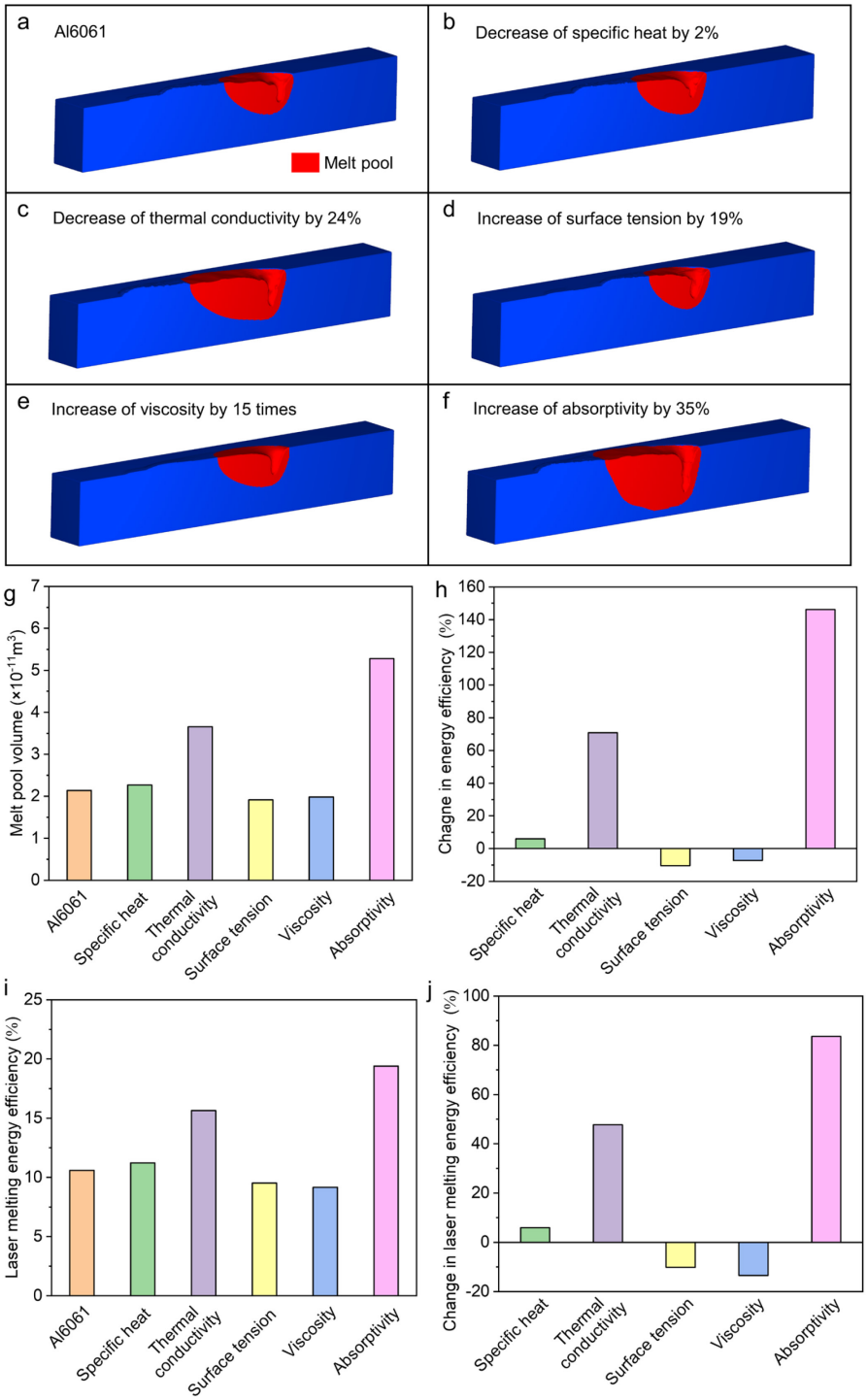

Fig. 5. Simulation results showing effects of property change caused by nanoparticles on melt pool volume and laser melting energy efficiency. *(a) Simulation of laser melting of Al6061. (b-f) Simulation of laser melting process using the nanoparticle-modified property of specific heat (b),*

thermal conductivity (c), surface tension (d), viscosity (e), and absorptivity (f). Other properties are from Al6061. The melt pool is indicated by the red color. (g) Effects of each property change on the melt pool volume. (h) Effects of each property change on the percentage change of melt pool volume compared with Al6061. (i) Effects of each property change on the laser melting energy efficiency. (j) Effects of each property change on the percentage change of laser melting energy efficiency compared with Al6061. The quantification of (g-j) was based on the vapor depression and melt pool dimension in simulation results.

Based on the vapor depression and melt pool dimension in simulation results, we calculated the effect of each property change on the laser melting energy efficiency. Consistent with the trend observed in the melt pool volume, we observed that nanoparticle-induced change of specific heat, thermal conductivity, surface tension, viscosity, absorptivity results in laser melting energy efficiency changes of 6%, 48%, -10%, -14%, 84%, respectively (Fig. 5i, j). This suggests that, among all the properties we measured, the nanoparticle-induced change of the absorptivity and thermal conductivity are the two main ones accounting for the improvement of the laser melting energy efficiency.

4.2. Effects of nanoparticle-induced reduction of vapor depression threshold on laser melting energy efficiency

Another mechanism we found for the nanoparticle-induced laser melting energy efficiency improvement is that adding nanoparticles reduces the laser power needed to generate the vapor depression. Since the laser power threshold for Al6061+4.4vol.%TiC to generate the vapor depression under 0.4 m/s scan speed was not captured within the utilized laser power range of 312 W to 520 W (Fig. 1), we performed further in-situ x-ray imaging experiments with laser power of 208 and 260 W. The results show that the minimum laser power needed for Al6061+4.4vol.%TiC to generate the vapor depression under 0.4 m/s scan speed is 260 W (Fig. 6a, b), compared with 416 W for Al6061 (Fig. 1). The same phenomenon that compared with Al6061, less laser power

was needed for Al6061+4.4vol.%TiC to generate the vapor depression was also observed under 0.6 m/s and 0.8 m/s scan speed (as detailed in Section 3.1 and Fig. 6d).

The nanoparticle induced vapor depression initiation under lower laser power results in a significant enhancement of the absorption for Al6061+4.4vol.%TiC under certain parameters (when Al6061 without vapor depression, Al6061+4.4vol.%TiC with vapor depression), due to the multiple reflection inside the vapor depression [37–39]. Therefore, under these parameters, there is a substantial increase of the melt pool volume and laser melting energy efficiency. The average laser melting energy efficiency increase (caused by the nanoparticles) is 268% under the condition of Al6061+4.4vol.%TiC with vapor depression but Al6061 without vapor depression, compared to 59% under the condition of both Al6061 and Al6061+4.4vol.%TiC with vapor depression or both without vapor depression (Fig. 6c).

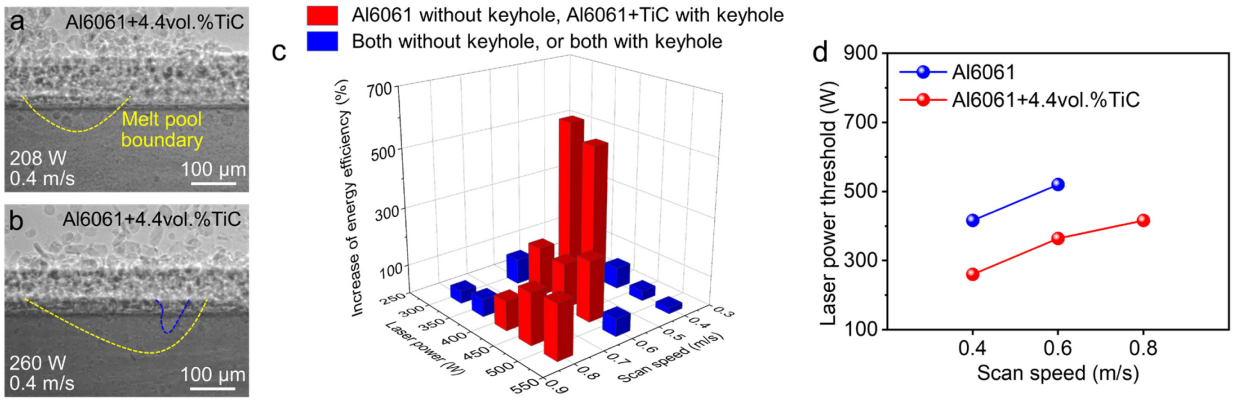

Fig. 6. Nanoparticle-enabled vapor depression initiation at lower laser power. *(a, b) X-ray images showing the laser power threshold for Al6061+4.4vol.%TiC to generate the vapor depression under laser scan speed of 0.4 m/s. In a, no vapor depression was generated at 208 W laser power. In b, vapor depression was generated at 260 W laser power. Blue dashed line indicates the vapor depression boundary. Yellow dashed lines indicate the melt pool boundary. (c) The laser melting energy efficiency increase induced by the nanoparticles under different laser processing parameters. Red columns represent the condition of Al6061+4.4vol.%TiC with vapor depression but Al6061 without vapor depression. Blue columns represent the condition of both Al6061 and Al6061+4.4vol.%TiC with vapor depression or both without vapor depression. (d) The laser power threshold for Al6061 and Al6061+4.4vol.%TiC to generate the vapor depression. Under 0.8 m/s scan speed, even though we used highest laser power of our laser system (520 W), no vapor depression was generated for Al6061.*

We propose that the nanoparticle-induced initiation of vapor depression at lower laser power is caused by the nanoparticle-induced increase of absorptivity and decrease of thermal conductivity. To study the effects of nanoparticle-induced absorptivity change and thermal conductivity change on the vapor depression initiation, we quantified the vapor depression depth as a function of time for three of the simulations mentioned in Section 4.1: (1) simulation using Al6061 properties, (2) simulation with 24% decrease of thermal conductivity, (3) simulation with 35% increase of absorptivity. The results show that decreasing the thermal conductivity and increasing the absorptivity both cause earlier initiation of the vapor depression (Fig. 7a).

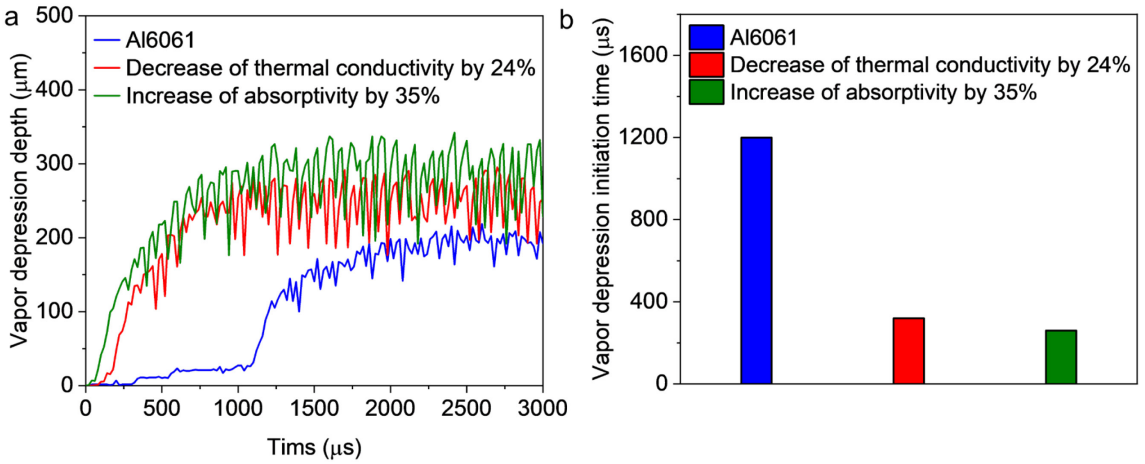

Fig. 7. Effects of nanoparticle-induced decrease of thermal conductivity and increase of absorptivity on vapor depression initiation. *(a), Vapor depression depth as a function of time obtained from laser melting simulation of Al6061, decreasing thermal conductivity by 24%, and increasing absorptivity by 35%. (b), The vapor depression initiation time obtained from laser melting simulation of Al6061, decreasing thermal conductivity by 24%, and increasing absorptivity by 35%.*

We calculated the initiation time of the vapor depression, which is defined as the time it takes for the vapor depression to reach half of the static vapor depression depth. The vapor depression initiation times after decreasing the thermal conductivity and increasing of the absorptivity are 320 μs and 260 μs, respectively, compared with the initiation time of 1200 μs for Al6061 (Fig. 7b).

This suggests that adding nanoparticles can facilitate the vapor depression initiation by increasing the absorptivity and decreasing the thermal conductivity.

Decreasing thermal conductivity can promote the vapor depression initiation because decreasing thermal conductivity reduces the heat dissipation, resulting in the fast increase of localized temperature and recoil pressure at melt pool surface to cause earlier initiation of vapor depression. When the absorptivity increases, it also causes the significant increase of the temperature at melt pool surface due to the larger amount of laser energy absorbed, which increases the recoil pressure and facilitates the vapor depression initiation.

4.3. Powder absorptivity or material absorptivity to affect melt pool dimension

Previous studies have demonstrated that adding nanoparticles in metal can increase the powder absorptivity (i.e., the absorptivity of the powder layer in LPBF) [30,40–43], and material absorptivity (i.e., the absorptivity of the flat surface) [10]. To find out which absorptivity should be used when studying nanoparticle effects on LPBF process, we further performed in-situ x-ray imaging experiments using bare substrates (Fig. 8), and then compare the experimental results using the bare substrate with those using the powder bed. The results indicate that whether the powder absorptivity or the material absorptivity should be used depends on whether the laser interacts with the powder or the liquid metal during the LPBF process.

In the keyhole mode where the laser mostly interacts with the liquid metal [57], the vapor depression and melt pool dimensions in the laser melting of bare substrate experiment are very close to those in the powder bed experiment for both Al6061 and Al6061+4.4vol.%TiC: the difference of the melt pool depth between the powder bed experiment and the bare substrate experiment is less than 10% for both Al6061 and Al6061+4.4vol.%TiC under all the parameters in the keyhole mode (Fig. 2d, Fig. 8d). More importantly, the nanoparticle-induced increase of

vapor depression depth and melt pool dimension was still observed in the laser bare substrate melting experiment (Fig. 8a-d). This suggests that powders have negligible effects, and the nanoparticle-induced material absorptivity enhancement should be used when studying nanoparticle effects on vapor depression and melt pool formation in keyhole mode.

In the conduction mode, laser interacts more with powders [58]. Therefore, the proportion of energy absorbed by powders in the overall absorption process increases. However, in the melt pool formation study, the powder absorptivity should only be used when (1) the laser mostly interacts with powders instead of liquid metal, (2) the laser-heated powders are finally merged into the melt pool instead of being ejected as spatters.

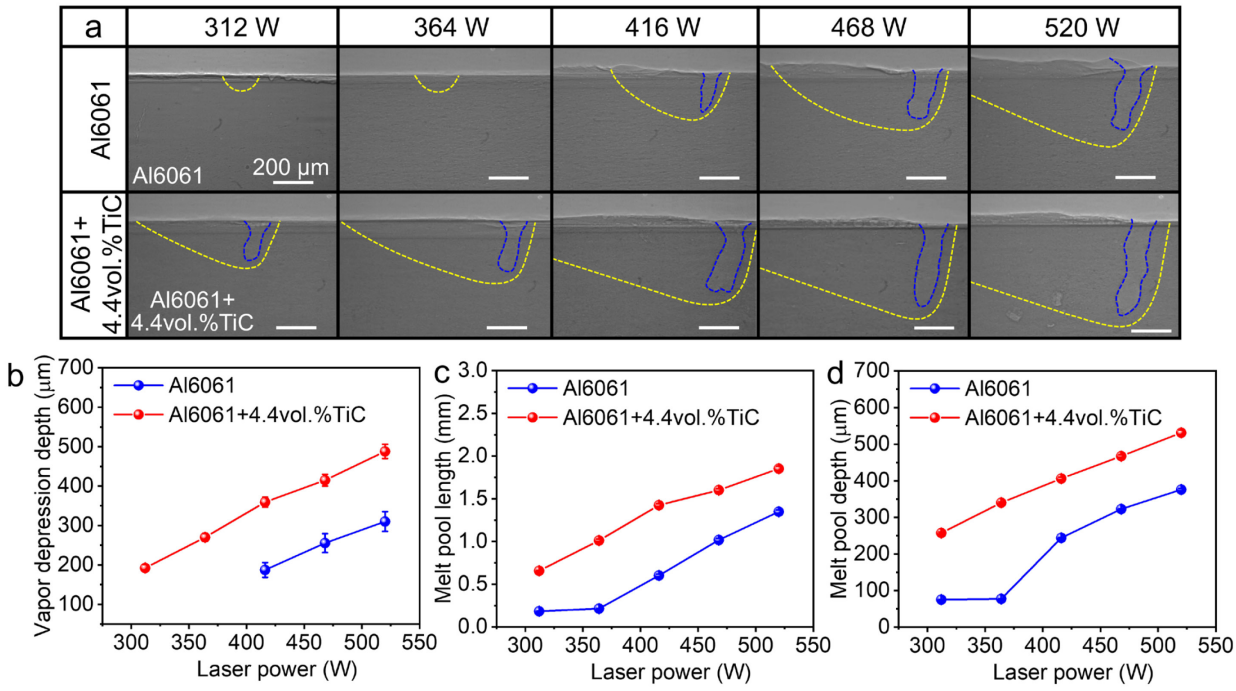

Fig. 8. Effects of nanoparticles on the vapor depression and melt pool dimension during laser melting of bare substrate. *(a) X-ray images showing the effects of nanoparticle on vapor depression and melt pool formation during laser melting of bare substrate. Blue dashed lines indicate the vapor depression boundary. Yellow dashed lines indicate the melt pool boundary. The laser powers used are 312 W, 364 W, 416 W, 468 W and 520 W. The scan speed used is 0.4 m/s. (b-d) Quantification results showing effects of nanoparticles on the vapor depression depth (b), melt pool length (c), and melt pool depth (d). The error bars represent the standard deviation.*

5. Conclusion

This work presents the quantification of the effects of TiC nanoparticles on the laser melting energy efficiency by direct characterization of vapor depression and melt pool dimension during LPBF of Al6061. A significant increase of laser melting energy efficiency is achieved by adding TiC nanoparticles. The mechanisms of laser melting energy efficiency improvement induced by TiC nanoparticles are identified. The major conclusions are as follows:

(1) We quantified the nanoparticle-induced improvement of laser melting energy efficiency by direct measurement of vapor depression and melt pool dimensions. The results show that adding TiC nanoparticles increased the laser melting energy efficiency by 114% on average under all the parameters we studied, and by 521% under 312 W laser power, 0.4 m/s scan speed during LPBF of Al6061.

(2) Among all the property changes caused by the TiC nanoparticles we studied, we identified that nanoparticle-induced increase of absorptivity and decrease of thermal conductivity play dominant role in increasing melt pool dimension and improving laser melting energy efficiency during LPBF of Al6061.

(3) In addition to the nanoparticle-induced property change, we found another mechanism causing the laser melting energy efficiency improvement during LPBF of Al6061: adding TiC nanoparticle enables the initiation of vapor depression at lower laser power (i.e., lowers the laser power threshold for keyholing), resulting in significant increase of laser melting energy efficiency through multiple reflection. The average laser melting energy efficiency increase (caused by the TiC nanoparticles) is 268% under the processing condition that Al6061+4.4vol.%TiC has vapor depression but Al6061 does not have vapor depression, which is much higher than the 59%

increase under the processing condition of both Al6061 and Al6061+4.4vol.%TiC with vapor depression or both without vapor depression.

(4) By comparing the laser powder bed experiment with laser bare substrate melting experiment, we further identified that powders have negligible effects in the keyhole mode. Therefore, the material absorptivity enhancement (instead of powder absorptivity enhancement) and thermal conductivity reduction induced by the TiC nanoparticles are the main mechanisms causing the increase of the vapor depression, melt pool dimensions and laser melting energy efficiency in keyhole-mode LPBF process.

Our research provides a potential method and mechanisms to increase the laser melting energy efficiency during laser metal AM process. More work will be done in the future to study the effects of different nanoparticles (with different thermophysical properties) and nanoparticle volume fraction on the laser melting efficiency to develop a general guideline for selecting/designing nanoparticles for different alloy systems to achieve more energy efficient laser metal AM process.

Acknowledgements

This work is supported by US National Science Foundation and University of Wisconsin-Madison Startup Fund. This research used resources of the Advanced Photon Source, a U.S. Department of Energy (DOE) Office of Science User Facility operated for the DOE Office of Science by Argonne National Laboratory under Contract No. DE-AC02-06CH11357.

Appendix A: Laser melting energy efficiency versus absorptivity

The term “laser melting energy efficiency” used in this paper is different from the “absorptivity” used in previous works. The definition of laser melting energy efficiency is the energy needed to melt the material to form a melt pool with a certain volume to the energy delivered by the laser beam. The melt volume formed does not only depend on the absorptivity. The thermal conductivity

(influencing heat dissipation to the substrate), the heat capacity, the viscosity (influencing the melt flow induced heat transfer within the melt pool) and surface tension (influencing the vapor depression development) also affect the melt pool volume. One of the major findings in our work is that adding nanoparticles can enlarge the melt pool volume under the same processing parameter. Also, we identify that apart from absorptivity increase, nanoparticle-induced decrease of thermal conductivity also makes significant contribution to the melt pool volume increase.

Therefore, we developed a new parameter of "laser melting energy efficiency" which directly connects the melt pool volume with laser energy input (Equation 14-15) by considering all the thermophysical properties governing the melt pool formation: except the absorptivity, it also considers thermal conductivity, specific heat, surface tension and viscosity. To further study the mechanism of nanoparticle-induced melt pool expansion, we systematically measured all the relevant thermophysical properties (absorptivity, thermal conductivity, specific heat, surface tension, viscosity) for the sample with and without nanoparticles and quantified their contribution to the melt pool volume and the laser melting energy efficiency. Compared with previous research studying nanoparticle-induced absorptivity change, our work using laser melting energy efficiency is a further study of effects of all the thermophysical property changes on the melt pool formation.

Appendix B: Melt pool length measurement

The melt pool length was measured based on the x-ray image. The horizontal length of the x-ray image view window is 1482 μm (768 pixels × 1.93 μm/pixel). For the melt pool length smaller than the horizontal length of x-ray imaging view window, we measured the melt pool length directly from the x-ray image (i.e., the number of pixels between the melt pool head and the melt pool end in the horizontal direction × 1.93 μm/pixel). For the melt pool length larger than the horizontal length of the field of view, the melt pool length is divided into two parts: (1) the length

of the melt pool portion displayed in the current field of view L_f, (2) the length of the rest of the melt pool beyond the field of view L_r. L_f is directly obtained from the x-ray image (Fig. B.1a). L_r is calculated by multiplying the melt pool moving speed (assumed the same as laser scan speed) and the time it takes for the rest of the melt pool moves into the field of view, as illustrated in Fig. B.1b. The total melt pool length was calculated as $L=L_f+L_r$.

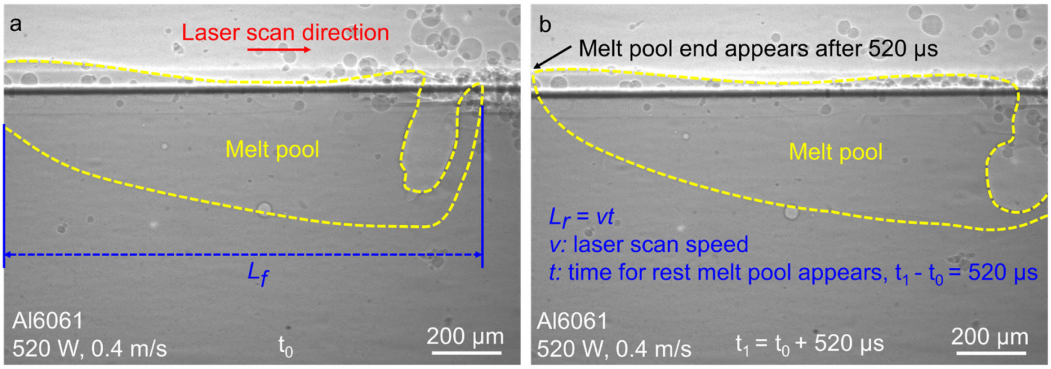

Fig. B.1. Melt pool length measurement. (a), X-ray image illustrating the measurement of L_f (the melt pool length in current frame). (b), X-ray image illustrating the calculation of L_r (the length of the rest of the melt pool). The total melt pool length is calculated as $L=L_f+L_r$.

Appendix C. Estimation of absorptivity based on the Fresnel equations

We estimated the material absorptivity of Al6061 and Al6061+TiC based on the refractive index and Fresnel equations. The absorptivity of Al6061 was calculated according to the Fresnel equation [59]:

$$A=1-(r_{TM}+r_{TE})/2 \tag{C.1}$$

$$r_{TM}=\frac{\left(n-\frac{1}{\cos\theta}\right)^2+k^2}{\left(n+\frac{1}{\cos\theta}\right)^2+k^2} \tag{C.2}$$

$$r_{TE}=\frac{(n-\cos\theta)^2+k^2}{(n+\cos\theta)^2+k^2} \tag{C.3}$$

where A is the absorptivity, r_{TM} is the reflectivity of the P polarization mode (TM, transverse-magnetic), r_{TE} is the reflectivity of the S polarization mode (TE, transverse-electric), θ is the incident angle, n and k are the real part and imaginary part of the complex refractive index, respectively. For Al, n = 1.37, k = 10.3 at 1070 nm wavelength [54].

The absorptivity of Al6061+TiC was calculated based on the mixture rule:

$$A_c = A_{Al}(1-f) + A_{TiC}f \quad \text{(C.4)}$$

where A_c is the absorptivity of Al6061+TiC, A_{Al} is the absorptivity of Al6061, f is the volume fraction of TiC, A_{TiC} is the absorptivity of TiC, which was calculated based on the Equation (C.1-C.3) and refractive index of TiC at 1070 nm wavelength (n=3.96, k=3.68 [60]). The calculated absorptivity of Al6061+4.4vol.%TiC is 32% higher (on average for all incident angles) than that of Al6061 (Fig. C.1), which is very close to the measurement results (absorptivity of Al6061+4.4vol.%TiC is 35% higher than that of Al6061) in Section 3.3.

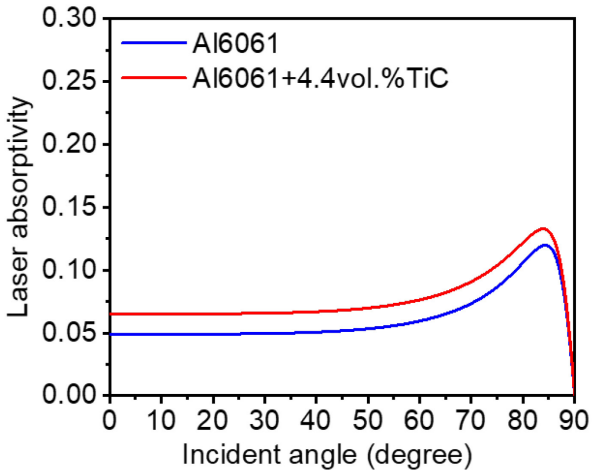

Fig. C.1. Laser absorptivity of Al6061 and Al6061+TiC estimated based on the refractive index and Fresnel equations.

Reference

[1] M.S. Pham, C. Liu, I. Todd, J. Lertthanasarn, Damage-tolerant architected materials

inspired by crystal microstructure, Nature. 565 (2019) 305–311. https://doi.org/10.1038/s41586-018-0850-3.
[2] T. Wohlers, Wohlers Report 2020: 3D Printing and Additive Manufacturing Global State of the Industry, Wohlers Associates, Inc., 2020.
[3] T. DebRoy, T. Mukherjee, H.L. Wei, J.W. Elmer, J.O. Milewski, Metallurgy, mechanistic models and machine learning in metal printing, Nat. Rev. Mater. 6 (2021) 48–68. https://doi.org/10.1038/s41578-020-00236-1.
[4] T. DebRoy, T. Mukherjee, J.O. Milewski, J.W. Elmer, B. Ribic, J.J. Blecher, W. Zhang, Scientific, technological and economic issues in metal printing and their solutions, Nat. Mater. 18 (2019) 1026–1032. https://doi.org/10.1038/s41563-019-0408-2.
[5] T. DebRoy, H.L. Wei, J.S. Zuback, T. Mukherjee, J.W. Elmer, J.O. Milewski, A.M. Beese, A. Wilson-Heid, A. De, W. Zhang, Additive manufacturing of metallic components – process, structure and properties, Prog. Mater. Sci. 92 (2018) 112–224. https://doi.org/10.1016/j.pmatsci.2017.10.001.
[6] T. Gutowski, S. Jiang, D. Cooper, G. Corman, M. Hausmann, J.A. Manson, T. Schudeleit, K. Wegener, M. Sabelle, J. Ramos-Grez, D.P. Sekulic, Note on the rate and energy efficiency limits for additive manufacturing, J. Ind. Ecol. 21 (2017) S69–S79. https://doi.org/10.1111/jiec.12664.
[7] K. Salonitis, Energy efficiency of metallic powder bed additive manufacturing processes, in: S.S. Muthu, M.M. Savalani, Handbook of Sustainability in Additive Manufacturing, Springer Singapore, Singapore, 2016, pp. 1–29. https://doi.org/10.1007/978-981-10-0606-7_1.
[8] Z.Y. Liu, C. Li, X.Y. Fang, Y.B. Guo, Energy consumption in additive manufacturing of metal parts, 26 (2018) 834–845. https://doi.org/10.1016/j.promfg.2018.07.104.
[9] S. Kou, Welding metallurgy, Wiley Interscience, New Jersey, 2003.
[10] O.A. Tertuliano, P.J. DePond, D. Doan, M.J. Matthews, X.W. Gu, W. Cai, A.J. Lew, Nanoparticle-enhanced absorptivity of copper during laser powder bed fusion, Addit. Manuf. 51 (2022) 102562. https://doi.org/10.1016/j.addma.2021.102562.
[11] S.D. Jadhav, S. Dadbakhsh, L. Goossens, J.P. Kruth, J. Van Humbeeck, K. Vanmeensel, Influence of selective laser melting process parameters on texture evolution in pure copper, J. Mater. Process. Technol. 270 (2019) 47–58. https://doi.org/10.1016/j.jmatprotec.2019.02.022.
[12] Q. Han, R. Setchi, F. Lacan, D. Gu, S.L. Evans, Selective laser melting of advanced Al-Al2O3 nanocomposites: Simulation, microstructure and mechanical properties, Mater. Sci. Eng. A. 698 (2017) 162–173. https://doi.org/10.1016/j.msea.2017.05.061.
[13] Z. Wang, T.A. Palmer, A.M. Beese, Effect of processing parameters on microstructure and tensile properties of austenitic stainless steel 304L made by directed energy deposition additive manufacturing, Acta Mater. 110 (2016) 226–235. https://doi.org/10.1016/j.actamat.2016.03.019.
[14] Q. Guo, C. Zhao, M. Qu, L. Xiong, L.I. Escano, S.M.H. Hojjatzadeh, N.D. Parab, K. Fezzaa, W. Everhart, T. Sun, L. Chen, In-situ characterization and quantification of melt pool variation under constant input energy density in laser powder bed fusion additive manufacturing process, Addit. Manuf. 28 (2019) 600–609. https://doi.org/10.1016/j.addma.2019.04.021.
[15] R.R. Unocic, J.N. DuPont, Process efficiency measurements in the laser engineered net shaping process, Metall. Mater. Trans. B. 35 (2004) 143–152.

https://doi.org/10.1007/s11663-004-0104-7.
[16] P. Kürnsteiner, M.B. Wilms, A. Weisheit, B. Gault, E.A. Jägle, D. Raabe, High-strength Damascus steel by additive manufacturing, Nature. 582 (2020) 515–519. https://doi.org/10.1038/s41586-020-2409-3.
[17] M. Tang, P.C. Pistorius, J.L. Beuth, Prediction of lack-of-fusion porosity for powder bed fusion, Addit. Manuf. 14 (2017) 39–48. https://doi.org/10.1016/j.addma.2016.12.001.
[18] P. Bidare, I. Bitharas, R.M. Ward, M.M. Attallah, A.J. Moore, Fluid and particle dynamics in laser powder bed fusion, Acta Mater. 142 (2018) 107–120. https://doi.org/10.1016/j.actamat.2017.09.051.
[19] U. Scipioni Bertoli, G. Guss, S. Wu, M.J. Matthews, J.M. Schoenung, In-situ characterization of laser-powder interaction and cooling rates through high-speed imaging of powder bed fusion additive manufacturing, Mater. Des. 135 (2017) 385–396. https://doi.org/10.1016/j.matdes.2017.09.044.
[20] H. Krauss, T. Zeugner, M.F. Zaeh, Layerwise monitoring of the Selective Laser Melting process by thermography, Phys. Procedia. 56 (2014) 64–71. https://doi.org/10.1016/j.phpro.2014.08.097.
[21] C. Zhao, K. Fezzaa, R.W. Cunningham, H. Wen, F. De Carlo, L. Chen, A.D. Rollett, T. Sun, Real-time monitoring of laser powder bed fusion process using high-speed X-ray imaging and diffraction, Sci. Rep. 7 (2017) 3602. https://doi.org/10.1038/s41598-017-03761-2.
[22] M. Qu, Q. Guo, L.I. Escano, J. Yuan, S.M.H. Hojjatzadh, S.J. Clark, K. Fezzaa, T. Sun, L. Chen, Controlling melt flow by nanoparticles to eliminate surface wave induced surface fluctuation, Addit. Manuf. 59 (2022) 130873. https://doi.org/10.1016/j.addma.2022.103081.
[23] J.A. Kanko, A.P. Sibley, J.M. Fraser, In situ morphology-based defect detection of selective laser melting through inline coherent imaging, J. Mater. Process. Technol. 231 (2016) 488–500. https://doi.org/10.1016/j.jmatprotec.2015.12.024.
[24] T.R. Allen, W. Huang, J.R. Tanner, W. Tan, J.M. Fraser, B.J. Simonds, Energy-coupling mechanisms revealed through simultaneous keyhole depth and absorptance measurements during laser-metal processing, Phys. Rev. Appl. 13 (2020) 064070. https://doi.org/10.1103/PHYSREVAPPLIED.13.064070.
[25] C. Ma, J. Zhao, C. Cao, T.C. Lin, X. Li, Fundamental study on laser interactions with nanoparticles-reinforced metals-part II: Effect of nanoparticles on surface tension, viscosity, and laser melting, J. Manuf. Sci. Eng. 138 (2016) 121002. https://doi.org/10.1115/1.4033446.
[26] M. Qu, Q. Guo, L.I. Escano, A. Nabaa, S.M.H. Hojjatzadeh, Z.A. Young, L. Chen, Controlling process instability for defect lean metal additive manufacturing, Nat. Commun. 13 (2022) 1079. https://doi.org/10.1038/s41467-022-28649-2.
[27] B. Song, S. Dong, P. Coddet, G. Zhou, S. Ouyang, H. Liao, C. Coddet, Microstructure and tensile behavior of hybrid nano-micro SiC reinforced iron matrix composites produced by selective laser melting, J. Alloys Compd. 579 (2013) 415–421. https://doi.org/10.1016/j.jallcom.2013.06.087.
[28] L.Y. Chen, J.Y. Peng, J.Q. Xu, H. Choi, X.C. Li, Achieving uniform distribution and dispersion of a high percentage of nanoparticles in metal matrix nanocomposites by solidification processing, Scr. Mater. 69 (2013) 634–637. https://doi.org/10.1016/j.scriptamat.2013.07.016.

[29] C.L.A. Leung, I. Elizarova, M. Isaacs, S. Marathe, E. Saiz, P.D. Lee, Enhanced near-infrared absorption for laser powder bed fusion using reduced graphene oxide, Appl. Mater. Today. 23 (2021) 101009. https://doi.org/10.1016/j.apmt.2021.101009.
[30] S.Y. Zhou, Z.Y. Wang, Y. Su, H. Wang, G. Liu, T.T. Song, M. Yan, Effects of micron/submicron TiC on additively manufactured AlSi10Mg: a comprehensive study from computer simulation to mechanical and microstructural analysis, JOM. 72 (2020) 3693–3704. https://doi.org/10.1007/s11837-019-03984-w.
[31] T.C. Lin, C. Cao, M. Sokoluk, L. Jiang, X. Wang, J.M. Schoenung, E.J. Lavernia, X. Li, Aluminum with dispersed nanoparticles by laser additive manufacturing, Nat. Commun. 10 (2019) 4124. https://doi.org/10.1038/s41467-019-12047-2.
[32] A. Fathy, O. El-Kady, Thermal expansion and thermal conductivity characteristics of Cu-Al2O3 nanocomposites, Mater. Des. 46 (2013) 355–359. https://doi.org/10.1016/j.matdes.2012.10.042.
[33] C. Ma, J. Zhao, C. Cao, T.C. Lin, X. Li, Fundamental study on laser interactions with nanoparticles-reinforced metals part I: Effect of nanoparticles on optical reflectivity, specific heat, and thermal conductivity, J. Manuf. Sci. Eng. 138 (2016) 121001. https://doi.org/10.1115/1.4033392.
[34] W.H. Yu, S.L. Sing, C.K. Chua, C.N. Kuo, X.L. Tian, Particle-reinforced metal matrix nanocomposites fabricated by selective laser melting: A state of the art review, Prog. Mater. Sci. 104 (2019) 330–379. https://doi.org/10.1016/j.pmatsci.2019.04.006.
[35] J. Shi, Y. Wang, Development of metal matrix composites by laser-assisted additive manufacturing technologies: a review, J. Mater. Sci. 55 (2020) 9883–9917. https://doi.org/10.1007/s10853-020-04730-3.
[36] B. AlMangour, D. Grzesiak, T. Borkar, J.M. Yang, Densification behavior, microstructural evolution, and mechanical properties of TiC/316L stainless steel nanocomposites fabricated by selective laser melting, Mater. Des. 138 (2018) 119–128. https://doi.org/10.1016/j.matdes.2017.10.039.
[37] A.A. Martin, N.P. Calta, J.A. Hammons, S.A. Khairallah, M.H. Nielsen, R.M. Shuttlesworth, N. Sinclair, M.J. Matthews, J.R. Jeffries, T.M. Willey, J.R.I. Lee, Ultrafast dynamics of laser-metal interactions in additive manufacturing alloys captured by in situ X-ray imaging, Mater. Today Adv. 1 (2019) 100002. https://doi.org/10.1016/j.mtadv.2019.01.001.
[38] N. Kouraytem, X. Li, R. Cunningham, C. Zhao, N. Parab, T. Sun, A.D. Rollett, A.D. Spear, W. Tan, Effect of laser-matter interaction on molten pool flow and keyhole dynamics, Phys. Rev. Appl. 11 (2019) 064054. https://doi.org/10.1103/PhysRevApplied.11.064054.
[39] J.H. Cho, S.J. Na, Implementation of real-time multiple reflection and Fresnel absorption of laser beam in keyhole, J. Phys. D. Appl. Phys. 39 (2006) 5372–5378. https://doi.org/10.1088/0022-3727/39/24/039.
[40] W. Zhou, X. Sun, K. Kikuchi, N. Nomura, K. Yoshimi, A. Kawasaki, Carbon nanotubes as a unique agent to fabricate nanoceramic/metal composite powders for additive manufacturing, Mater. Des. 137 (2018) 276–285. https://doi.org/10.1016/j.matdes.2017.10.034.
[41] M. Chen, X. Li, G. Ji, Y. Wu, Z. Chen, W. Baekelant, K. Vanmeensel, H. Wang, J.P. Kruth, Novel composite powders with uniform TiB2 nano-particle distribution for 3D printing, Appl. Sci. 7 (2017) 250. https://doi.org/10.3390/app7030250.

[42] D. Gu, Y. Yang, L. Xi, J. Yang, M. Xia, Laser absorption behavior of randomly packed powder-bed during selective laser melting of SiC and TiB2 reinforced Al matrix composites, Opt. Laser Technol. 119 (2019) 105600. https://doi.org/10.1016/j.optlastec.2019.105600.
[43] X.P. Li, G. Ji, Z. Chen, A. Addad, Y. Wu, H.W. Wang, J. Vleugels, J. Van Humbeeck, J.P. Kruth, Selective laser melting of nano-TiB2 decorated AlSi10Mg alloy with high fracture strength and ductility, Acta Mater. 129 (2017) 183–193. https://doi.org/10.1016/j.actamat.2017.02.062.
[44] M. Qu, Q. Guo, L.I. Escano, S.J. Clark, K. Fezzaa, L. Chen, Mitigating keyhole pore formation by nanoparticles during laser powder bed fusion additive manufacturing, Addit. Manuf. Lett. 3 (2022) 100068. https://doi.org/10.1016/j.addlet.2022.100068.
[45] M. González-Cardel, P. Arguijo, R. Díaz-Uribe, Gaussian beam radius measurement with a knife-edge: A polynomial approximation to the inverse error function, Appl. Opt. 52 (2013) 3849–3855. https://doi.org/10.1364/AO.52.003849.
[46] W. Yan, W. Ge, Y. Qian, S. Lin, B. Zhou, W.K. Liu, F. Lin, G.J. Wagner, Multi-physics modeling of single/multiple-track defect mechanisms in electron beam selective melting, Acta Mater. 134 (2017) 324–333. https://doi.org/10.1016/j.actamat.2017.05.061.
[47] B. Jiang, K. Huang, Z. Cao, H. Zhu, Thermodynamic study of titanium oxycarbide, Metall. Mater. Trans. A. 43 (2012) 3510–3514. https://doi.org/10.1007/s11661-011-1032-1.
[48] H. Capacity, Flash method of determining thermal diffusivity, Encycl. Therm. Stress. 1679 (2014) 1683–1683. https://doi.org/10.1007/978-94-007-2739-7_100240.
[49] P. Yuan, D. Gu, Molten pool behaviour and its physical mechanism during selective laser melting of TiC/AlSi10Mg nanocomposites: Simulation and experiments, J. Phys. D. Appl. Phys. 48 (2015) 035303. https://doi.org/10.1088/0022-3727/48/3/035303.
[50] C.W. Nan, R. Birringer, D.R. Clarke, H. Gleiter, Effective thermal conductivity of particulate composites with interfacial thermal resistance, J. Appl. Phys. 81 (1997) 6692–6699. https://doi.org/10.1063/1.365209.
[51] A.E. Gheribi, P. Chartrand, Temperature and oxygen adsorption coupling effects upon the surface tension of liquid metals, Sci. Rep. 9 (2019) 7113. https://doi.org/10.1038/s41598-019-43500-3.
[52] E.S. Elton, T.C. Reeve, L.E. Thornley, I.D. Joshipura, P.H. Paul, A.J. Pascall, J.R. Jeffries, Dramatic effect of oxide on measured liquid metal rheology, J. Rheol. (N. Y. N. Y). 64 (2020) 119–128. https://doi.org/10.1122/1.5117144.
[53] B. Karlsson, J.E. Sundgren, B.O. Johansson, Optical constants and spectral selectivity of titanium carbonitrides, Thin Solid Films. 87 (1982) 181–187. https://doi.org/10.1016/0040-6090(82)90273-5.
[54] A.D. Rakić, Algorithm for the determination of intrinsic optical constants of metal films: application to aluminum, Appl. Opt. 34 (1995) 4755. https://doi.org/10.1364/ao.34.004755.
[55] B.J. Simonds, J. Tanner, A. Artusio-Glimpse, P.A. Williams, N. Parab, C. Zhao, T. Sun, The causal relationship between melt pool geometry and energy absorption measured in real time during laser-based manufacturing, Appl. Mater. Today. 23 (2021) 101049. https://doi.org/10.1016/j.apmt.2021.101049.
[56] M. Matthews, J. Trapp, G. Guss, A. Rubenchik, Direct measurements of laser absorptivity during metal melt pool formation associated with powder bed fusion additive

manufacturing processes, J. Laser Appl. 30 (2018) 032302. https://doi.org/10.2351/1.5040636.
[57] C. Zhao, N.D. Parab, X. Li, K. Fezzaa, W. Tan, A.D. Rollett, T. Sun, Critical instability at moving keyhole tip generates porosity in laser melting, Science. 370 (2020) 1080–1086. https://doi.org/10.1126/science.abd1587.
[58] J. Trapp, A.M. Rubenchik, G. Guss, M.J. Matthews, In situ absorptivity measurements of metallic powders during laser powder-bed fusion additive manufacturing, Appl. Mater. Today. 9 (2017) 341–349. https://doi.org/10.1016/j.apmt.2017.08.006.
[59] Y. Yang, D. Gu, D. Dai, C. Ma, Laser energy absorption behavior of powder particles using ray tracing method during selective laser melting additive manufacturing of aluminum alloy, Mater. Des. 143 (2018) 12–19. https://doi.org/10.1016/j.matdes.2018.01.043.
[60] D.W. Lynch, C.G. Olson, D.J. Peterman, J.H. Weaver, Optical properties of TiCx(0.64≤x≤0.90) from 0.1 to 30 eV, Phys. Rev. B. 22 (1980) 3991.

CRediT author statement

Minglei Qu: Conceptualization, Formal analysis, Investigation, Methodology, Writing – original draft, Writing – review & editing. **Qilin Guo:** Investigation, Methodology. **Luis I. Escano:** Investigation. **Ali Nabaa:** Investigation. **Kamel Fezzaa:** Investigation. **Lianyi Chen:** Conceptualization, Supervision, Funding acquisition, Investigation, Methodology, Project administration, Resources, Writing – review & editing.